 FDMP, vol.9, no.4, pp.435-460, 2013

Computational Studies on the Transient Electrohydrodynamics of a Liquid Drop

Md. Abdul Halim[1] **and Asghar Esmaeeli**[2]

Abstract: This study aims to gain a detailed understanding of the transient behavior of solitary liquid drops in electric fields at finite Reynolds number. A front tracking/finite difference method, in conjunction with Taylor-Melcher leaky dielectric model, is used to solve the governing electrohydrodynamic equations. The evolution of the flow field and drop deformation is studied for a few representative fluid systems, corresponding to the different regions of the deformation-circulation map. It is shown that for the range of the physical parameters used here, the deformation-time history is governed by one time scale while the fluid flow (characterized by kinetic energy) is governed by two or more time scales. The effect of the material property ratios and the wall on the electrohydrodynamics of the drop is also investigated.

1 Introduction

The steady state electrohydrodynamics (EHD) of a liquid drop suspended in another liquid and exposed to a weak uniform electric field is reasonably well understood. Taylor (1966) was the first in formulating the problem analytically by considering creeping flow and zero deformation, who in the process laid out a framework that later on became known as "Taylor-Melcher leaky dielectric" model (Melcher and Taylor, 1969; Saville, 1997). Briefly, under a weak electric field the drop remains spherical or deforms to an ellipsoid whose major axis is in the direction of or perpendicular to the field. Furthermore, a circulatory flow, in the form of toroidal vortices, is established inside and outside of the drop. The deformation and fluid flow circulation is due to mismatch of the dielectric properties (i.e., electric conductivity and permittivity) of the fluids inside and outside of the drop, which leads to electric stresses at the surface of the drop. These stresses tend to deform the drop and set the fluid in motion at the interface.

[1] Department of Mechanical Engineering & Energy Processes, Southern Illinois University, Carbondale, IL 62901.

[2] Corresponding author. Tel.: 618-453-7001; Fax: 618-453-7001; E-mail: esmaeeli@engr.siu.edu

Following the seminal work of Taylor (1966), there have been several major studies concerning the steady state behavior of a drop. Here we do not attempt to review the literature, instead we refer to two comprehensive theoretical studies in this regard. Feng and Scott (1996) present a nice review of the state of understanding of the problem beginning with the studies based on the electrohydrostatic (EHS) model, which were customarily used a decade or so before the leaky-dielectric model came to existence, and the follow up studies after Taylor (1966) up to their own study. These authors used Galerkin finite element method and performed comprehensive parametric study to characterize the effect of fluid inertia on the deformation of the drop. They also determined the critical electric strength beyond which an equilibrium solution does not exit. More recently, Lac and Homsy (2007) performed boundary integral calculations for various regions of the parameter space, assuming creeping flow conditions, and identified the various equilibrium shapes or breakup modes (i.e., tip-streaming, bulbous breakup from the middle, etc) of a drop.

While the steady state EHD of a drop is reasonably well-understood, not much is known about its transient behavior. This understanding finds relevance in a host of microfluidic applications such as enhancement of mixing by electric forces (Stone *et al.*, 2004) where information about the relative importance of the pertinent time scales of the phenomena compared to the time scale of the process of interest, and the manner in which the flow develops is a key to the optimum design and performance of the device. Here the theoretical results are mostly limited to a few studies based on analytical and semi-analytical solutions of the equations for creeping flow regime and nearly spherical drops. A review of the literature in this regard can be found in Esmaeeli and Sharifi (2011). Briefly, for fluid systems where flow Reynolds number $Re_f = \rho u_s a/\mu$ and Ohnesorge number $Oh = \mu/\sqrt{\rho a \gamma}$ are small, the convective term $(\mathbf{u}\cdot\nabla\mathbf{u})$ and the temporal acceleration term $\partial\mathbf{u}/\partial t$ in the Navier-Stokes equation can be ignored and the drop dynamics depends on one time scale only, which is the deformation time scale that governs the relaxation of the drop and the velocity field toward steady state. On the other hand, if $Re_f \ll 1$ but $Oh \not\ll 1$, the convective term can be ignored while the acceleration term cannot. In this case, the dynamics will be governed by two time scales. Of particular relevance to this work, is the analytical solution for the deformation of a liquid column (i.e., a 2D drop) by Esmaeeli and Sharifi (2011). These authors assumed $Re_f \ll 1$ and $Oh \ll 1$ and derived a closed form solution for the velocity field and deformation. Specifically, they showed that the deformation-time history of a drop is governed by the following equation:

$$\mathscr{D} = \mathscr{D}_\infty \Big[1 - \exp(-t/\tau)\Big], \tag{1}$$

$$\tau = \frac{(\mu_i + \mu_o)a}{\gamma}, \tag{2}$$

$$\mathscr{D} = \frac{y_{max} - x_{max}}{y_{max} + x_{max}}. \tag{3}$$

Here, $\mathscr{D}$ is the deformation parameter, τ is the characteristic time, and $\mathscr{D}_\infty$ is the steady state deformation. x_{max} and y_{max} are are the end-to-end length of the cylinder cross section in the direction of electric field and the maximum breadth in the traverse direction, respectively. The steady state deformation is found using $\mathscr{D}_\infty = (Ca/3)[\Phi/(R+1)^2]$, according to Reddy and Esmaeeli (2009). Here, $\Phi = R^2 + R + 1 - 3S$ is a characteristic function that determines the sense of deformation of the drop (i.e., oblate vs. prolate), $Ca = \mu u_s/\gamma$ is the capillary number, and R and S are the electric conductivity and permittivity ratios (inside over the outside), respectively.

While the studies pertaining to evolution of nearly spherical drops in creeping flow provides a good insight about the transient behaviors, in a large class of practical applications the inertia becomes important and the deformation cannot be ignored. Furthermore, even for the steady state behavior of a single drop, it seems that the effect of fluid properties, and the wall effects have not been studied in a systematic way. Our goal is to shed some light on these less-explored aspects using Direct Numerical Simulations. While the computations are performed for two-dimensional systems, the results are applicable for three-dimensional systems in a "qualitative" sense.

2 Problem Setup and Nondimensional Parameters

The problem setup is shown in Fig. (1), depicting an initially circular drop of radius a in a pool of another liquid. The electric field is established by assigning electric potentials ϕ_t and ϕ_b to the top and the bottom walls, respectively. The computational domain is periodic in the horizontal direction and wall-bounded in the vertical direction. No-slip and no-through flow boundary conditions are used for the velocity field at the walls and periodic boundary conditions are used in the horizontal direction.

The physical properties of the fluids are the densities, ρ_i, ρ_o, the viscosities, μ_i, μ_o, the electric permittivities, ε_i, ε_o, and the electric conductivities, σ_i, σ_o. The surface tension is γ. The subscripts i and o denote the physical parameters inside and outside of the drop, respectively. The gravity is set to zero. The governing nondimensional numbers of this problem are $Re_f = \rho_o u_s a/\mu_o$, $Ca = \mu_o u_s/\gamma$, $\alpha = \pi a^2/WH$, $R = \sigma_i/\sigma_o$, $S = \varepsilon_i/\varepsilon_o$, $\widetilde{\rho} = \rho_i/\rho_o$, and $\widetilde{\mu} = \mu_i/\mu_o$. Here, Re_f, Ca, and α are, respectively, the flow Reynolds number, the capillary number, and the volume

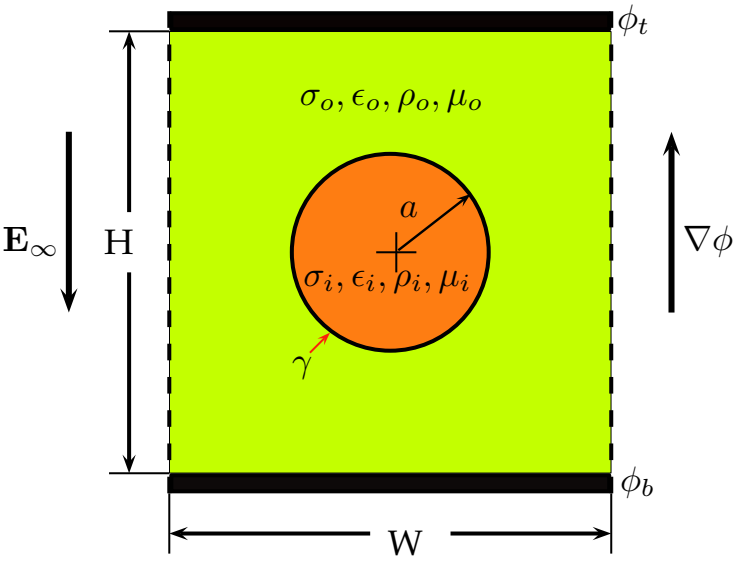

Figure 1: The computational setup, depicting a liquid drop of radius a immersed in another liquid. Here ρ, μ, σ, and ε represents, respectively, the density, the viscosity, the electric conductivity, and the electric permittivity. The computational domain is wall-bounded and periodic in the vertical and the horizontal direction, respectively.

fraction. $u_s = \varepsilon_o E_0^2 a/\mu_o$ is a velocity scale that is constructed by balance of the electric and viscous shear stresses at the surface of the drop and $E_0 = |\phi_t - \phi_b|/H$ is a characteristic scale for the electric field strength. Sometimes in the literature, the Ohnesorge number $Oh = \mu_o/\sqrt{\rho_o a \gamma}$, or the nondimensional strength of the electric field $E^* = \sqrt{Ca} = E_0/\sqrt{\gamma/\varepsilon_o a}$ are used in lieu of the Re_f and Ca, respectively. For leaky dielectric model to be valid, the time scale of charge relaxation from the bulk to the surface of the drop (i.e., maximum of $\tau_{C_i} = \varepsilon_i/\sigma_i$ and $\tau_{C_o} = \varepsilon_o/\sigma_o$) should be much shorter than any process time of interest τ_P. The ratio of τ_C over τ_P is called the electric Reynolds number Re_{el}, and thus it should be very small. Here, the convective time scale is the process time of interest, $\tau_P = a/u_s$, and the electric Reynolds number in our simulations is $Re_{el_o} = \varepsilon_o u_s/\sigma_o a = 0.005 \ll 1$. When we present our results, unless mentioned otherwise, we will use u_s, a, and $t_s = a/u_s$ as our velocity, length, and time scales.

3 Mathematical Formulation

Electrohydrodynamics deals with interactions of electric field and fluid flow. As such, the laws concerning the fluid dynamics and electric field and their coupling need to be considered. Here, the governing equations are the conservations of mass and momentum, and simplified Maxwell's electromagnetic equations. For leaky dielectric fluids with constant properties and net zero charge in the bulk, it can be shown that the electric field equations are decoupled from the fluid flow equations, but the fluid flow equations are coupled to the electric field equations through the momentum jump conditions (Melcher and Taylor, 1969; Saville, 1997). This decoupling allows one to solve the electric field and fluid dynamics equations sequentially.

Rather than writing the governing equations separately for each phase, we use a "one-fluid" formulation, where a single set of equations is written for all the fluids/phases involved, and the phase boundary is treated as an embedded interface by adding the appropriate source terms to the conservation laws. These source terms are in the form of delta-functions localized at the interface and are selected in such a way to satisfy the correct matching conditions at the phase boundary. Here, we are concerned with incompressible, immiscible, and Newtonian fluids. The resulting "one-fluid" Navier-Stokes equation governing the entire domain is:

$$\rho\left(\frac{\partial \mathbf{u}}{\partial t}+\nabla\cdot(\mathbf{uu})\right)=-\nabla p+\nabla\cdot[\mu(\nabla\mathbf{u}+(\nabla\mathbf{u})^T)]+\gamma\int_S \kappa_f \mathbf{n}_f \delta(\mathbf{x}-\mathbf{x}_f)dS_f+\mathbf{F}_e. \tag{4}$$

This equation is similar to the conventional Navier-Stokes equation except for the two terms on the right hand side which account for the effect of surface tension and electric field, respectively. Note that the gravity is zero in our simulations. The force due to the surface tension is represented by the integral over the surface of the phase boundary; γ is the surface tension coefficient, κ is twice the mean curvature in two dimensions, $\mathbf{n}$ is a normal unit vector at the interface, δ is a two-dimensional delta function, and dS is the differential surface element of the interface. The variables with subscript f are evaluated at the interface; $\mathbf{x}$ is the point at which the equation is evaluated and $\mathbf{x}_f$ is the position of a point at the interface.

To calculate $\mathbf{F}_e$, we need to calculate the electric potential ϕ first. This is done in one-fluid formulation by solving the following equation

$$\nabla\cdot\sigma\nabla\phi=0, \tag{5}$$

and then computing the electric field strength using $\mathbf{E}=-\nabla\phi$. The electric force

is calculated using $\mathbf{F}_e = \nabla \cdot \tau^e$, where τ^e is the Maxwell stress tensor:

$$\tau^e = \varepsilon \mathbf{E}\mathbf{E} - \frac{1}{2}\mathbf{I}\mathbf{E}\cdot\mathbf{E}. \tag{6}$$

The momentum equation is supplemented by the mass conservation equation, which for incompressible flows is simply:

$$\nabla \cdot \mathbf{u} = 0. \tag{7}$$

It is important to recognize that the single-field formulation satisfies the conventional governing equations and naturally incorporates the correct jump conditions across the interface. Specifically, the mass conservation leads to

$$[\![\mathbf{u}]\!] \cdot \mathbf{n} = 0, \tag{8}$$

the Navier-Stokes equation yields

$$[\![\tau^h - p\mathbf{I}]\!] \cdot \mathbf{n} + [\![\tau^e]\!] \cdot \mathbf{n} + \gamma\kappa\mathbf{n} = 0, \tag{9}$$

and the electric field equation results in

$$[\![\phi]\!] = 0; \quad [\![\sigma\nabla\phi]\!] \cdot \mathbf{n} = 0. \tag{10}$$

Here, $[\![Q]\!] = Q_o - Q_i$ represent the jump in a typical variable Q across the interface. The key parameters that affect the sense of interface deformation and fluid circulation are the net normal and tangential electric traction forces at the interface; i.e., $[\![\tau^e_{nn}]\!]$ and $[\![\tau^e_{tn}]\!]$, respectively. Using Maxwell stresses and the continuity of the electric current density at the interface, it can be shown that the net normal and tangential electric stresses are

$$[\![\tau^e_{nn}]\!] = \frac{\varepsilon_o}{2}\left[\left(1 - \frac{S}{R^2}\right)E^2_{n_o} + (S-1)E^2_t\right], \tag{11}$$

and

$$[\![\tau^e_{tn}]\!] = \varepsilon_o E_{n_o} E_t \left(1 - \frac{S}{R}\right) = q_s E_t, \tag{12}$$

respectively, q_s being the free electric charge at the surface. Here, these stresses are presented in terms of tangent-normal $t-n$ coordinates so that they can be used for a general orthogonal coordinate system. Note that subscript "o" stands for the outside and $E_{t_i} = E_{t_o} \equiv E_t$. For a spherical (circular) drop in three (two) dimensional spherical (polar) coordinates $t \equiv \theta$ and $n \equiv r$. As is seen, both components of the

electric field contribute to the net normal and tangential stresses. The action of the electric field on free surface charge can lead to both normal and tangential forces at the interface. The free surface charge can be found from

$$q_s = \varepsilon_o E_{n_o} \left(1 - \frac{S}{R}\right). \tag{13}$$

See, Reddy and Esmaeeli (2009) for more detail. It should be noted that in the one-fluid formulation, the net electric stresses are implicitly enforced through the calculation of $\mathbf{F}_e = \nabla \cdot \tau$ and the surface charge is found using $q_s = \nabla \cdot (\varepsilon \mathbf{E})$.

4 Numerical Method

We use a well-established numerical method to solve the governing equations. In the absence of the electric field, the method is described in detail in the review article by Tryggvason *et al.* (2001). Here, we briefly describe the extensions of the method for incorporation of electric field effects. We work with two sets of grids: a stationary grid and a moving/unstructured grid. The stationary grid is used to discretize the governing equations. The moving grid marks the position of the phase boundary and is used to keep the stratification of material properties sharp and to calculate the surface tension. This grid is also used to advect the fluid/fluid phase boundary by interpolating the velocities of the marker points from the regular grid. The computations start with meshing the surface of the interface using small line segments and assigning the materials properties (ρ, μ, σ, and ε) of both fluids. We then solve equation (5) for the electric potential and find the electric field using $\mathbf{E} = -\nabla\phi$. Maxwell stress τ^e is then found using Eq. (6) and the electric force is found by taking the gradient of the electric stress $\mathbf{F}_e = \nabla \cdot \tau^e$. This force is then added to the right hand side of the Navier-Stokes equation. To solve the Navier-Stokes equation, we use a standard projection algorithm where we split the momentum equation into two parts. The first part is a prediction step where the effect of pressure is ignored:

$$\frac{\mathbf{u}^* - \mathbf{u}^n}{\Delta t} = \frac{1}{\rho^n}\mathbf{A}(\mathbf{u}^n), \tag{14}$$

and the second part is a correction step where the pressure gradient is added:

$$\frac{\mathbf{u}^{n+1} - \mathbf{u}^*}{\Delta t} = -\frac{1}{\rho^n}\nabla_h p. \tag{15}$$

Here, $\mathbf{A}$ is a term that bulks the discrete advection, diffusion, surface tension, and electric force terms in the Navier-Stokes equations, and $\mathbf{u}^*$ is a provisional velocity

field in the absence of pressure. Subscript h denotes the finite difference numerical approximation. The pressure is determined in such a way that the velocity at the next time step is divergence free:

$$\nabla_h \cdot \mathbf{u}^{n+1} = 0 \tag{16}$$

To find the pressure, we take the divergence of equation (15) and using equation (16) yields

$$\nabla_h \cdot \left(\frac{1}{\rho^n} \nabla_h p \right) = \frac{\nabla_h \cdot \mathbf{u}^*}{\Delta t}. \tag{17}$$

Equation (17) is solved using a multigrid iteration method and the velocity field is corrected by including the pressure effects:

$$\mathbf{u}^{n+1} = \mathbf{u}^* - \frac{1}{\rho^n} \Delta t \nabla_h p. \tag{18}$$

The method as described above is first order in time and second order accurate in space. However, in numerical implementation, we use a predictor/corrector algorithm that makes the method second order accurate in time (Esmaeeli and Tryggvason, 2004).

5 Results and Discussion

To study the transient behavior of liquid drops, it will be quite helpful to predict their steady state behavior using the so-called deformation-circulation map. This map is constructed in a $R-S$ coordinates according to the asymptotic solution (i.e., creeping flow, zero deformation) of Taylor (1966) or Reddy and Esmaeeli (2009) for drops in three- or two-dimensional system, respectively. The map was initially used by Torza *et al.* (1971) to interpret their experimental and analytical results. Baygents *et al.* (1998) also used the map to predict the interactions of two tandem or side-by-side drops. Figure (2) shows the map for a drop in two-dimensional systems, which is based on the solution of Rhodes *et al.* (1989). Here the straight line is the so-called zero-circulation line, where $R = S$ and the charge distribution at the surface of the drop vanishes. Along this line the fluid flow cease to exist at equilibrium, since $R = S$ is tantamount to a perfect dielectric fluid system. The curve is the so-called zero-deformation curve and represents the solution of $\Phi \equiv R^2 + R + 1 - 3S = 0$, where Φ is called the deformation characteristic function. For more detail, see, Reddy and Esmaeeli (2009). The $\Phi = 0$ curve and the $R = S$ line divide the domain into three regions, identified as region I, II, and III, respectively. In region (I), $\Phi < 0$ and $R < S$; the drop deforms to an oblate ellipse (an ellipse

with its major axis perpendicular to the field) and the ambient fluid flows from the top/bottome (poles) toward the sides (equator). In region (II), $\Phi > 0$ and $R < S$; the drop deforms to a prolate ellipse (an ellipse with its major axis in the direction of the field) and the ambient fluid flows from the poles toward the equator. Finally, in region (III), $\Phi > 0$, and $R > S$; the drop deforms to a prolate ellipse (an ellipse with its major axis in the direction of the field) and the ambient fluid flows from the equator toward the poles.

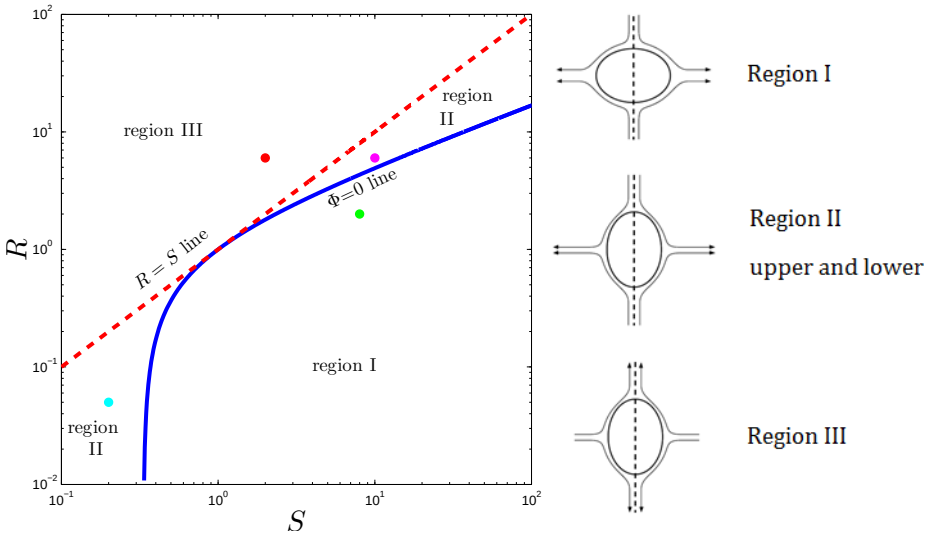

Figure 2: Circulation-deformation map.

5.1 Comparison of Representative Cases from The Map

5.1.1 Flow Patterns and Deformation Modes

We performed four simulations to explore the transient behaviors of the drops in the various regions of the map; one simulation each in regions (I) and (III), and two simulations in region (II); one simulation in the upper region and another one in the lower region. The coordinates of these simulations in the map are marked with solid circles. For all the simulations, $Re_f = 1$, $Ca = 0.25$, $\alpha = 0.1256$, $Oh_o = 0.5$, $Oh_i = 0.71$, $\widetilde{\rho} = 0.5$, and $\widetilde{\mu} = 1$. So, the main difference from one simulation to another is the difference in the conductivity and permittivity ratios; R and S,

respectively. For all the simulations, the computational domain is $2.5d \times 2.5d$, where d is the initial diameter of the drop and the grid resolution is 256×256.

We start our analysis by considering the behavior of a drop in region (I). Here, $R = 2$ and $S = 8$ and it is expected the drop to deform to an oblate shape and the ambient fluid flows from the poles toward the equator at steady state. Figure (3) shows two frames from the evolution of the velocity field and the drop and one frame from the streamlines at a steady state. The flow field is stronger at the surface of the drop compared with the rest of the domain, because the flow initiates there and propagates to the rest of the domain. Both the net normal and tangential electric stresses contribute initially to the velocity field because of the deformation of the interface. However, at steady state where the drop does not deform any longer, the velocity field is driven solely by the net tangential electric stresses. Initially four vortices are formed outside of the drop near the surface and the velocity vectors cross the surface of the drop. As the time progresses, the vortices gradually move outward and the velocity field inside the drop becomes weaker. At steady state, the velocity field consists of four closed vortices inside the drop that are matched by their counterparts in the outside. The structure of the vortices at steady state can be seen better by inspection of the streamlines. The fact that no streamline crosses the drop is an evident that the interface does not deform any more.

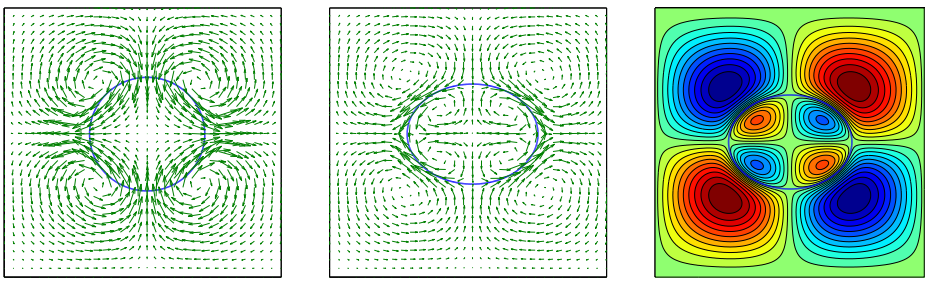

Figure 3: Evolution of the velocity field and the streamlines for a single drop in DC field (region I). Here, $Re_f = 1$, $Ca_{el} = 0.25$, $R = 2$, $S = 8$, $\widetilde{\mu} = 1$, and $\widetilde{\rho} = 0.5$.

Considering the direction of the ambient flow around the drop, it is clear that the fluid flow (i.e., normal hydrodynamic stresses) tends to deform the drop to an oblate. However, it should be noted that the deformation of the drop is the result of the combined action of the net normal hydrodynamic $[\![\tau^h_{nn}]\!]$ and $[\![\tau^e_{nn}]\!]$ electric stresses. Thus, from the direction of the flow field alone it is not possible to predict with certainty the sense of deformation of the drop. This point can be clarified

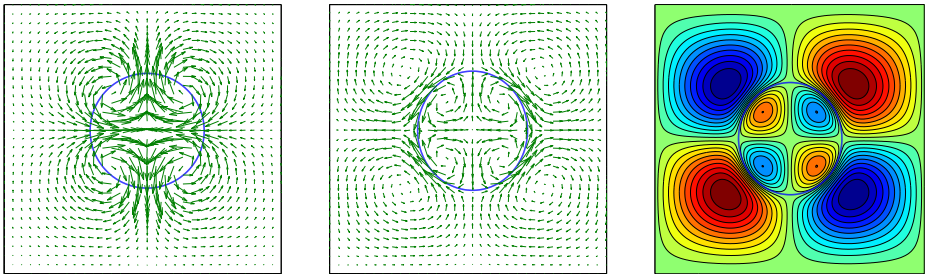

Figure 4: Evolution of the drops and the velocity field for a single drop in DC field (region II - upper). Here, $Re_f = 1$, $Re_{el} = 0.005$, $Ca_{el} = 0.25$, $R = 6$, $S = 10$, $\widetilde{\mu} = 1$ and $\widetilde{\rho} = 0.5$.

better by considering the flow field and the drop deformation for the simulations performed in region (II). Fig. (4) shows two selected frames of the velocity field for this simulation, one at an early time and another one at a steady state. The last frame shows the streamlines at a steady state. Here, $R = 6$ and $S = 10$ and it is expected that the drop deforms to a prolate shape and the fluid flows from the poles toward the equator. Note that this case corresponds to the upper part of region (II). Judging by the structure of the velocity field at steady state it is evident that the flow field tends to deform the drop to an oblate shape. However, considering the fact that the actual steady state shape of the drop is a prolate it can be conjectured that the net normal electric stresses have been larger in this case and their senses are opposite to that of the hydrodynamic stresses.

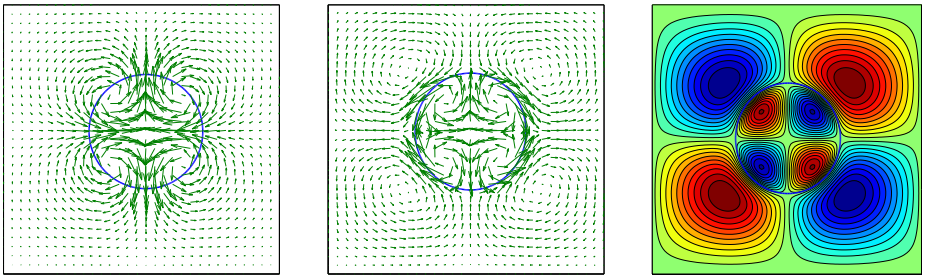

Figure 5: Evolution of the velocity field and streamlines for a single drop in DC field (region II-lower). Here, $Re_f = 1$, $Ca_{el} = 0.25$, $R = 0.05$, $S = 0.2$, $\widetilde{\mu} = 1$, and $\widetilde{\rho} = 0.5$.

We also performed anther simulation in the lower region, where $R = 0.05$ and $S = 0.2$. Figure (5) shows two frames for the velocity field (at an early time and a steady state time) and the streamlines at steady state. As is evident, the steady state flow pattern and the deformation are similar to the corresponding values in the upper region.

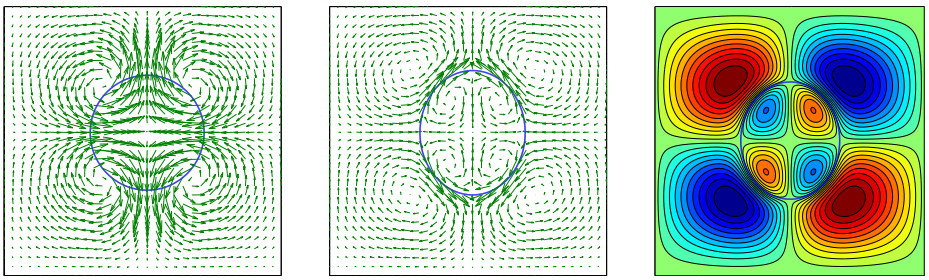

Figure 6: Evolution of the velocity field and streamlines for a single drop in DC field (region III). Here, $Re_f = 1$, $Ca_{el} = 0.25$, $R = 6$, $S = 2$, $\widetilde{\mu} = 1$, and $\widetilde{\rho} = 0.5$.

Figure (6) shows two selected frames for the velocity field for a simulation in region (III). Here, $R = 6$ and $S = 2$ and it is expected that the drop deforms to a prolate shape and the fluid flows from the equator to the poles. From the direction of the flow pattern it is seen that the flow tends to deform the drop to a prolate. Evaluation of the net normal electric stresses (Eq. 11) also suggests that these stresses tend to deform the drop to a prolate. Considering the fact that both of the net normal stresses are in the same direction, it is expected that the deformation of the drop in this region will be larger than that for a drop in region (II) under comparable condition.

5.1.2 Electric Potential, Electric Strength, and Free Surface Charge

The structure of the electric potential ϕ around the surfaces of the drop is of interest, as it affects the strength and distribution of the free electric charge and the electric stresses, which control the intensity of fluid circulation and degree of drop deformation. Fig. (7) shows contours of the electric potentials for the four cases. For the simulations in regions (I), (II-upper), and (III), $R > 1$, therefore, the electric potential is weaker inside the drop compared to the outside and the electric potential gradient is higher around the surface. Furthermore, the contourlines around the drop surface conform to the pertinent surfaces. This is not the case for region (II-lower), where $R < 1$. Here, the contourlines cross the interface and the electric potential gradient is weaker around the surface.

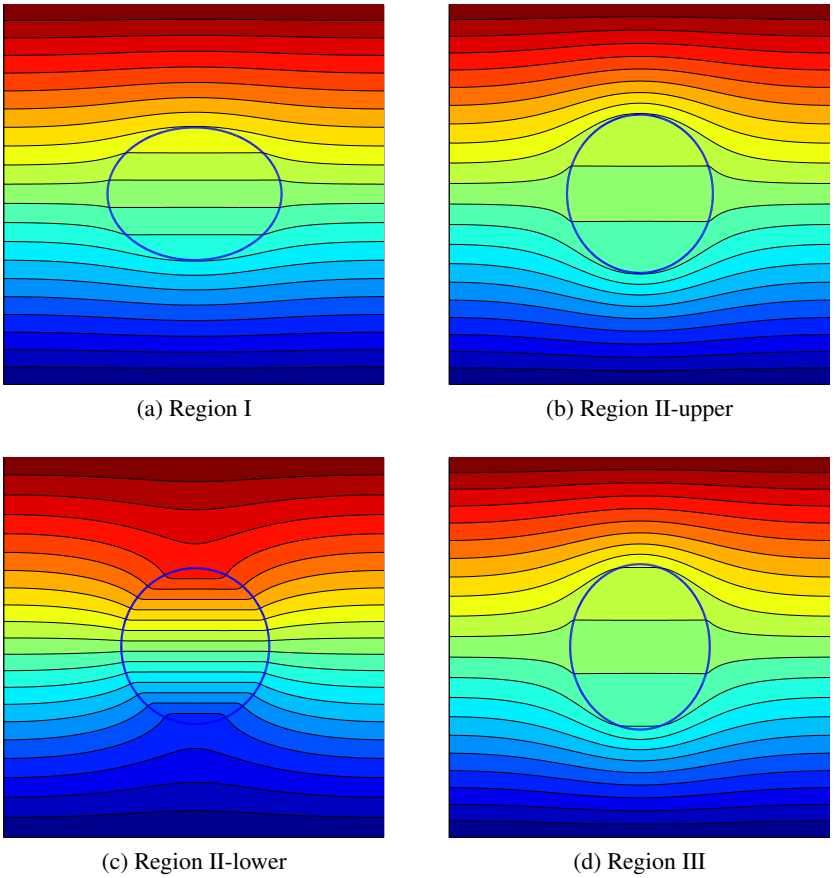

(a) Region I (b) Region II-upper

(c) Region II-lower (d) Region III

Figure 7: Contours of electric potential for a single drop in DC field for the four different regions.

Fig. (8) shows the vectors of the electric field strength for these cases. For all the cases, the electric field is uniform inside the drop and away from it. For the three cases in region (I), (II-upper), and (III), the vectors in the ambient fluid cross the drop, while for case (II-lower), the vectors conform to the surface and change their way as they come close to the surface. It should be noted that in general the electric field streamlines are orthonormal to the electric potential contours (Behjatian and Esmaeeli, 2011).

Fig. (9) shows the contours of electric surface charge. Here the red and blue colors

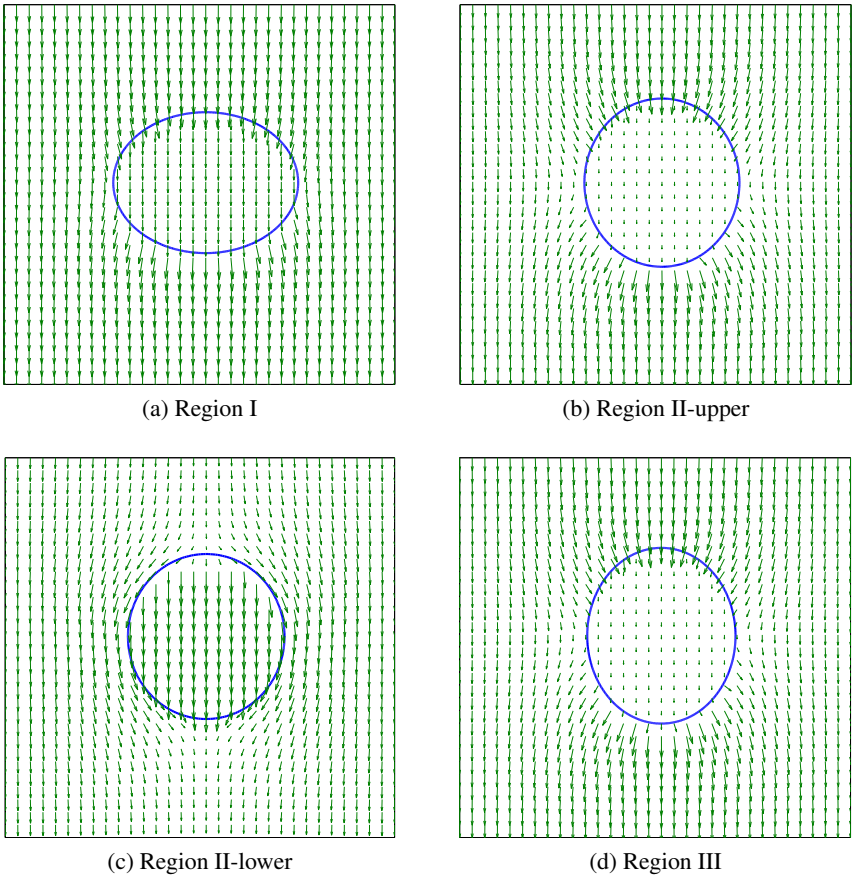

(a) Region I (b) Region II-upper

(c) Region II-lower (d) Region III

Figure 8: Vectors of electric field **E** for a single drop in DC field for the four different regions.

represent, respectively, the positive and the negative charges. The concentration of the contourlines represent the strength of the electric charge. As is evident, the charge is nearly zero at the sides and its magnitude (in an absolute sense) increases toward the poles. For the simulations in regions (I), (II-upper), and (II-lower), where $R < S$, positive charges are induced at the upper half of the drop (which faces the positive electrode) and negative charges are induced at the lower half (which faces the negative electrode). For these cases, the electric shear stress tends to drive the flow from the poles toward the equator. Conversely, for the simulation in region (III), where $R > S$, negative charges are induced at the upper half of the

drop (which faces the positive electrode) and positive charges are induced at the lower half (which faces the negative electrode). For this case, the electric shear stress tends to drive the flow from the equator toward the poles.

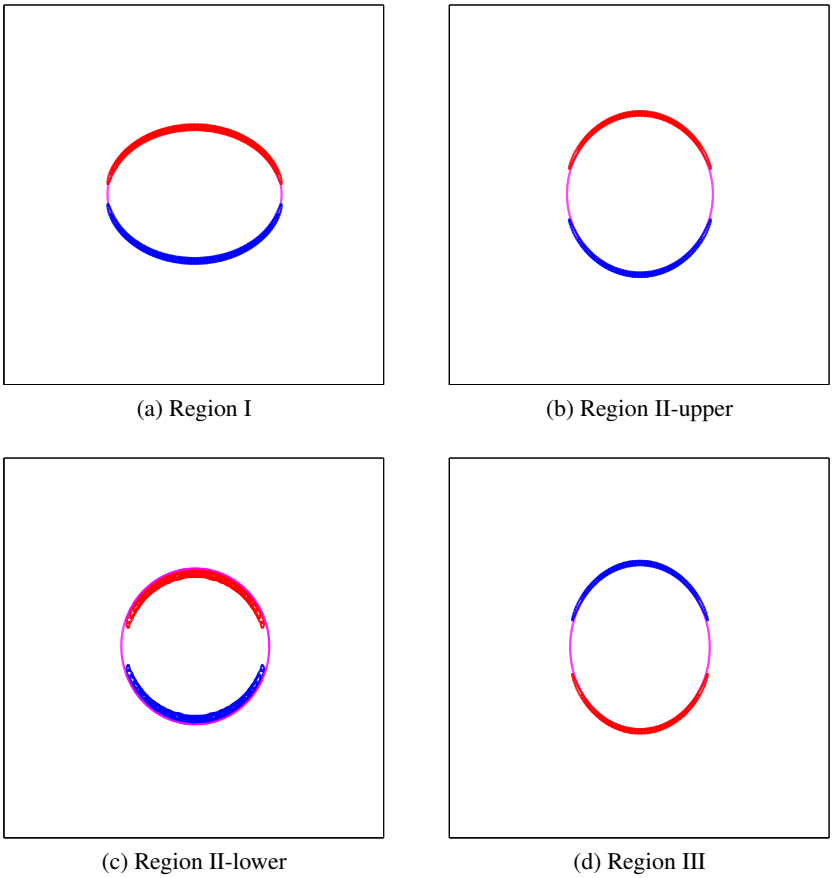

(a) Region I

(b) Region II-upper

(c) Region II-lower

(d) Region III

Figure 9: Contours of electric charge for a single drop in DC field for the four different regions.

5.1.3 Deformation and Kinetic Energy Time History

The evolution of the drop shape and the velocity field toward the steady state provides interesting insight about the transient behavior. Here, we explore these parameters by calculating the deformation parameter $\mathscr{D}$ and the kinetic energy. The

deformation parameter is found by approximating the drop with an ellipse with the same surface area, calculation of the second moments of inertia of the drop (numerically) and finding the major and minor axes. The kinetic energy is calculated using $KE = (1/2)\int_A \rho(u^2+v^2)dA$, where u and v are the components of the velocity field in the horizontal and the vertical direction, and A is the area of the computational domain. The kinetic energy is scaled with $\rho_o u_s^2 A$, where $u_s = \varepsilon_o E_0^2 a/\mu_o$ is the velocity scale. The time is nondimensionalized with $\tau_d = \mu_o a/\gamma$ which is a time scale of surface deformation (see, Esmaeeli and Sharifi, 2011).

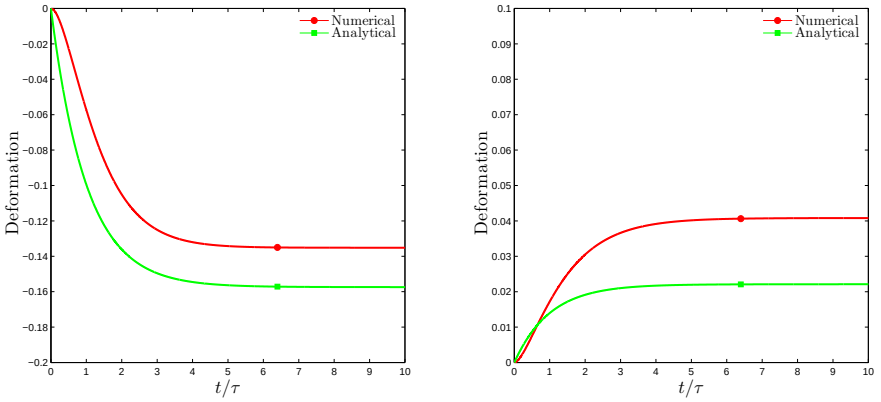

(a) Region I

(b) Region II-upper

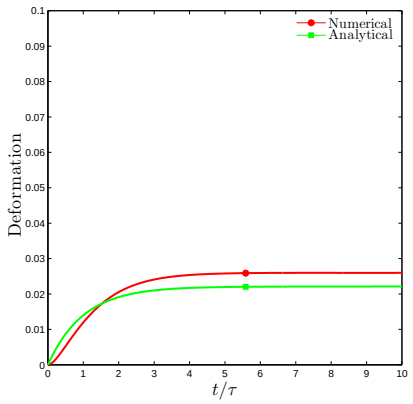

(c) Region II-lower

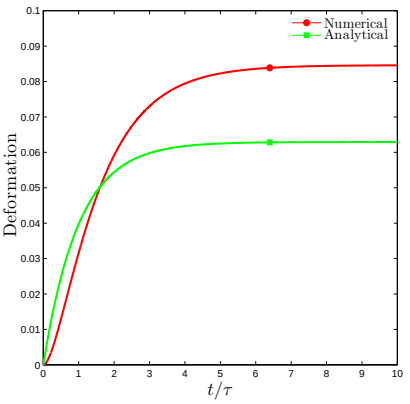

(d) Region III

Figure 10: Comparisons of the numerical and the analytical deformations for a single drop in DC field for the four different regions. Here time is scaled with $\tau_d = a\mu_o/\gamma$.

Fig. (10) shows the deformation time history for the drop in the four regions along with the prediction from creeping flow solution of Esmaeeli and Sharifi (2011). In all the cases, the drop deformation evolves monotonically toward the steady state, which suggest that the surface deformation is governed only by one time scale. Furthermore, the analytical solution always underpredicts the deformation, which is understandable considering the fact that fluid inertia, as measured by $Re_f = 1$, is not weak in our calculation. It can be conjectured, however, that the time scales of the drop deformation toward the steady state are nearly the same in both numerical and analytical results.

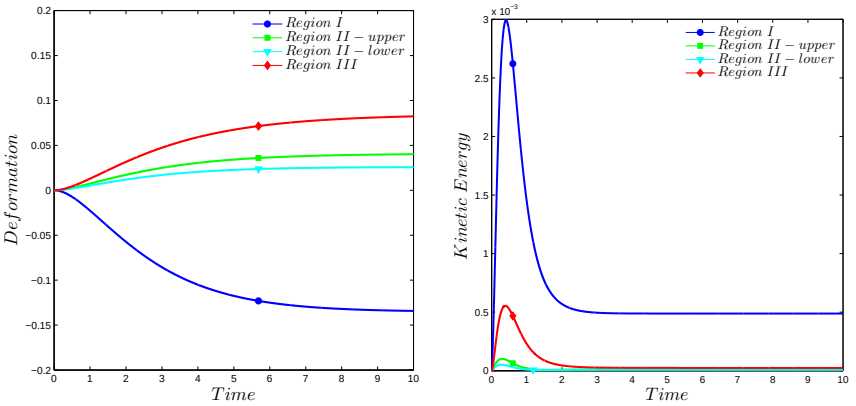

(a) Deformation vs. time

(b) Kinetic energy vs. time

Figure 11: Comparisons of the deformation (left frame) and the kinetic energy (right frame) for a single drop in DC field for the four different regions. Here the deformation is scaled with $\tau_d = \mu_o a/\gamma$ and the kinetic energy is scaled with $t_s = a/u_s$.

Fig. (11) compares the deformation parameter and the kinetic energy for the four cases. Again, $\tau_d = \mu_o a/\gamma$ is used to nondimensionalize the time. The figure suggests that the relaxation time toward steady state for all the cases is nearly the same. The order of the deformation parameter in an absolute sense, from maximum to minimum, is regions (I), (III), (II-upper), and (II-lower). Considering the deformation parameter predicted by the creeping flow solution

$$\mathscr{D} = \frac{Ca}{3}\frac{\Phi}{(R+1)^2}, \tag{19}$$

where $Ca = \mu_o u_s/\gamma$ and $\Phi = R^2 + R + 1 - 3S$, it is seen that Ca number is the same

for all the cases. Thus, the difference in the deformation parameter boils down to the difference in $\Phi/(R+1)^2$. The magnitude of this parameter in an absolute sense is $|-1.89|$, 0.755, 0.41, and 0.265 for regions (I), (III), (II-lower), and (II-upper), respectively. Thus, while the numerical and the analytical results agree in the relative order of the deformation parameters of the drop in regions (I) and (III), they disagree on the order of the deformation in the other two regions. Considering the fact that the magnitudes of the numerical deformation for these two regions are close, and that the kinetic energy of the flow in region (II-upper) is slightly higher than that in region (II-lower), it can be conjectured that the inertia effects are responsible for this discrepancy. While the deformation parameter increases monotonically toward the steady state, the kinetic energy increase from zero to a maximum and then settles to a steady state that is much smaller than that of the maximum value. This is because the fluid velocity is controlled by two time scales, the deformation time scale $\tau_d = \mu_o a/\gamma$ and the diffusion time scale $\tau_\mu = a^2/\nu_o$, where $\nu = \mu/\rho$. Here the kinetic energy reaches a maximum corresponding to the shorter time scale and then settles to a steady, corresponding to the larger time scale.

5.2 Effect of Ratio of Material Properties

In this section we investigate the effect of the material properties on the deformation and kinetic energy time history. Here, a reference simulation is considered where the non-dimensional parameters are $Re_f = 1$, $Ca_{el} = 0.25$, $Oh_i = 0.71$, $Oh_o = 0.5$, $\alpha = 0.1256$, $R = 2.5$, $S = 0.5$, $\widetilde{\mu} = 1$, and $\widetilde{\rho} = 0.5$. To study the effect, one of the non-dimensional parameters is changed at a time while keeping all the others the same. In all the cases considered, the time scale of the deformation-time and kinetic energy-time curves are nondimensionalized by $\tau_d = \mu_o a/\gamma$ (the deformation time scale) and $t_s = a/u_s$ (the convective time scale), respectively.

5.2.1 Effect of Electric Conductivity Ratio R

Here, we performed five simulations, including the reference simulation, to explore the effect of this parameter. Fig. (12) shows the results. As is evident, both the deformation and the kinetic energy increase with an increase in R. This observation can be justified by considering Eqs. (11)-(13). An increase in R, while keeping the permittivity ratio S constant, is tantamount to an increase in the net normal and tangential electric stresses. The former is the key parameter in setting the sense and the magnitude of the deformation and the latter is the key parameter in setting the strength of the flow field.

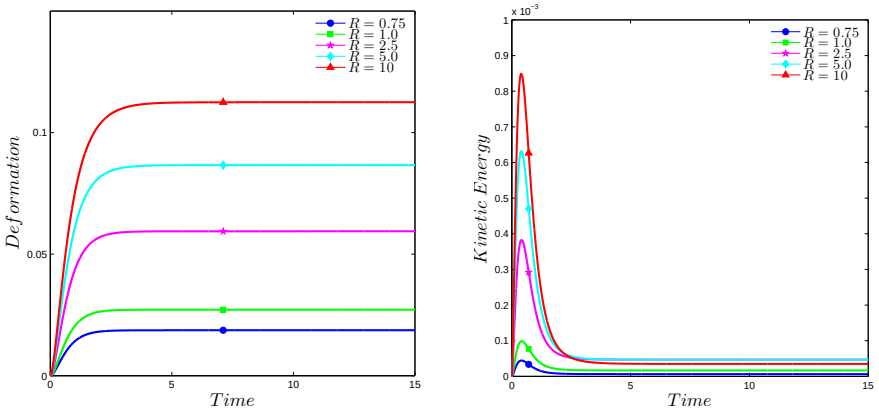

Figure 12: Effect of conductivity ratio (R) on drop dynamics. Here the deformation is scaled with $\tau_d = \mu_o a/\gamma$ and the kinetic energy is scaled with $t_s = a/u_s$.

5.2.2 *Effect of Electric Permittivity Ratio S*

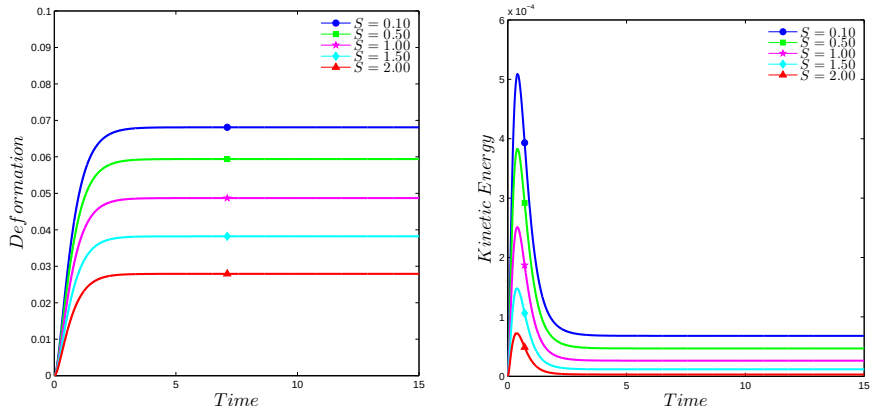

Figure 13: Effect of permittivity ratio (S) on drop dynamics. Here the deformation is scaled with $\tau_d = a\mu_o/\gamma$ and the kinetic energy is scaled with $t_s = a/u_s$.

Here, we performed five simulations, including the reference simulation, to explore the effect of this parameter. Fig. (13) shows the results. The deformation parameter decreases with an increase in S, while the kinetic energy increases with an increase

in S. Again, this observation is in line with the predictions from the net normal and tangential electric stresses at the interface. An increase in S, decreases the first term in Eq. (11) while it increase the second term. The final outcome depends on the balance of the two terms. Judging by the results here, it can be conjectured that the decrease in the magnitude of the first component has been larger than that of the increase in the second component and, therefore, the overall effect has been to reduce the net normal electric stresses. On the other hand, an increase in S can lead to a reduction in the magnitude of the net tangential electric stresses up to a point and a change of sign and increase (in an absolute sense) of the magnitude of these stresses. Since kinetic energy calculation is silent about the change in the direction of the flow field, we only can see the net effect which is an increase in the kinetic energy.

5.2.3 Effect of Viscosity Ratio $\widetilde{\mu}$

Here, we performed five simulations, including the reference simulation, to explore the effect of this parameter. Fig. (14) shows the results. The deformation parameter increases with an increase in $\widetilde{\mu}$, while the kinetic energy decreases. The increase in deformation of a drop due to an increase in the viscosity ratio has been observed at creeping flow studies in the context of shear-driven flows (see, for example, Stone, 1994). The decrease in the kinetic energy is as expected since an increase in the overall viscosity $\mu_i + \mu_o$ will lead to more flow dissipation. Here, the interesting observation is the time scale of relaxation toward steady state, after the peak, in the kinetic energy-time curve, where it is seen that the time scales are nearly the same. Furthermore, the maximum kinetic energy decreases as the viscosity ratio increases.

5.2.4 Effect of Density Ratio $\widetilde{\rho}$

Here, we performed three simulations, including the reference simulation, to explore the effect of this parameter. Fig. (15) shows the results. As is evident, an order of magnitude change in the density ratio essentially does not influence the results for the range of nondimensional parameters considered. It is seen that this parameter slightly affects the magnitude of the deformation during the transient rather than the steady state. Also, increasing $\widetilde{\rho}$ leads to a slight increase in the kinetic energy.

5.3 The Wall Effect

In the simulations so far, the drop was initially placed in the middle of the domain and did not move because of the geometrical and physical symmetries. The ques-

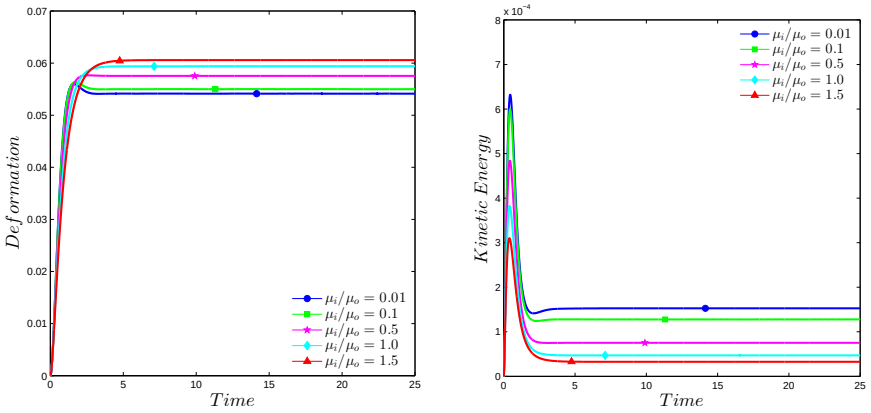

Figure 14: Effect of viscosity ratio $(\widetilde{\mu})$ on drop dynamics. Here the deformation is scaled with $\tau_d = a\mu_o/\gamma$ and the kinetic energy is scaled with $t_s = a/u_s$.

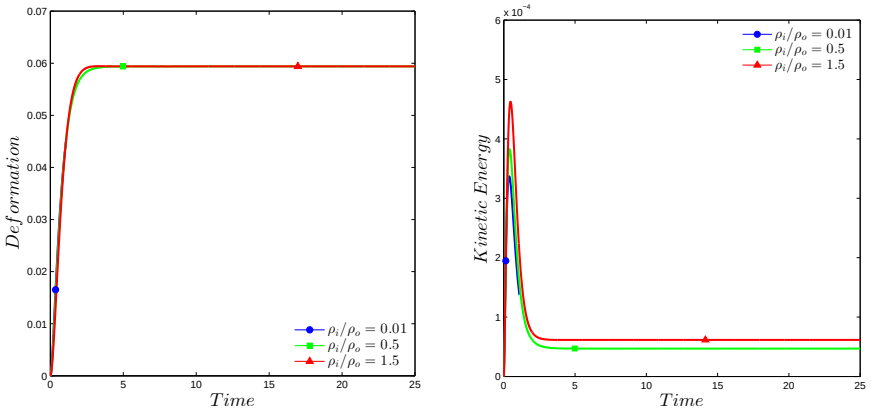

Figure 15: Effect of density ratio $(\widetilde{\rho})$ on drop dynamics. Here the deformation is scaled with $\tau_d = a\mu_o/\gamma$ and the kinetic energy is scaled with $t_s = a/u_s$.

tion that naturally arises is that what happens when the drop is not symmetrically placed with respect to the electrodes.

To answer this question, we performed a number of simulations in the four different regions of the map, where we followed the motion of a drop when it was initially placed closer to one of the walls. The horizontal position of the center of the drop was symmetric with respect to the left and the right boundaries, so that the drop

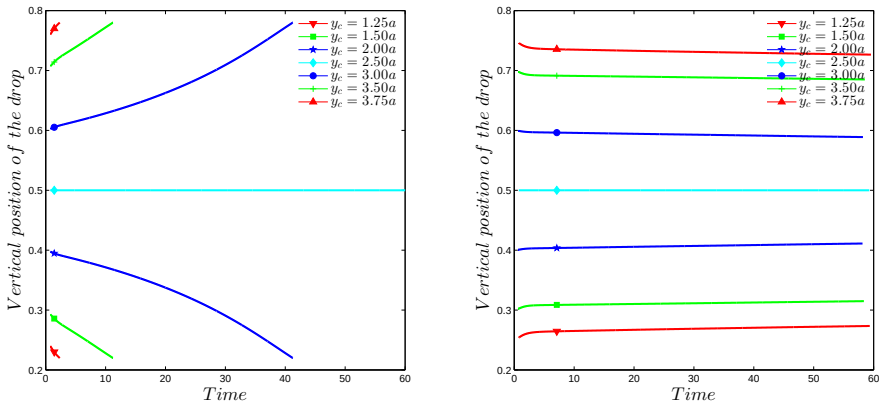

(a) Region-I (b) Region-III

Figure 16: Effect of vertical position on the drop dynamics for Region I and III, respectively. Here the time is scaled with $t_s = a/u_s$.

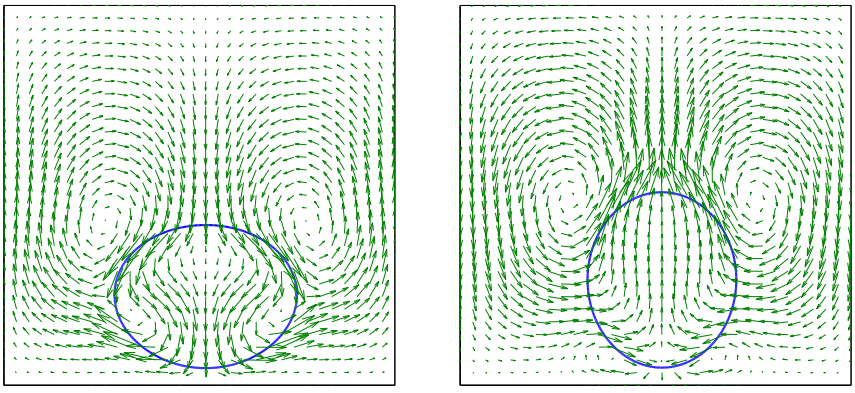

(a) Region I (b) Region III

Figure 17: Evolution of the velocity vectors for a drop placed at a distance of $y_c = 1.25a$ from the bottom wall for Region I and III, respectively.

would not move in the horizontal direction. Here, we describe the results of two sets of these simulations for a drop in regions (I) and (III). The nondimensional numbers for these simulations were the same as those used earlier in this study. Fig. (16) shows the evolution of the vertical position of the drops with time. It is seen that the drop in region (I) is attracted toward the walls while the drop in

region (III) is repelled from the wall. Simulations of drops in regions (II-upper) and (II-lower) also showed that the drops would be attracted toward the wall. To find the justification, we examined the velocity fields of the drops in these cases. Figure (17) shows the velocity fields for the two cases. As is evident, for both cases, the velocity field around the drop is stronger in the region that is further away from the wall compared with the region that is near the wall. This yields a higher hydrodynamic force in the former region compared with that in the latter. Thus, the motion of the drop toward or away from the wall is dictated by the direction of the ambient velocity field in the region away from the wall. For the drops in region (I), (II-upper), and (II-lower), where the flow is from the poles to the equator, the drop will be always attracted to the wall. For the drops in region (III), where the sense of the flow is the opposite, the drop will be always repelled from the wall.

6 Conclusion

Transient EHD behaviors of solitary drops in a uniform DC electric field was studied using Direct Numerical Simulations. A front tracking/finite difference method was used in conjunction with Taylor-Melcher's leaky dielectric model. Representative simulations for the four regions of the deformation-circulation map showed that steady state behavior of the drops is in line with the prediction of asymptotic theory (Taylor, 1966, for a three-dimensional drop; Reddy and Esmaeeli, 2009, for a two-dimensional drop). Initially four vortices appeared around the surface of the drop in the ambient, and retreated toward the outside as the time progressed. Eventually, the core of vortices settled to equilibrium positions in the ambient fluids and were matched by four counterpart vortices inside the drop. The sense of circulation and deformation at steady state depended on the relative importance of R and S. For $R < S$, the flow was from the poles toward the equator, while the reverse was true for $R > S$. The sense of deformation at steady state was in line with the sense of the characteristic deformation function $\Phi = R^2 + R + 1 - 3S$ for two-dimensional systems. The effects of the material properties were studied. Briefly, it was shown that for the range of the parameters used here, kinetic energy KE increased with an increase in R or S. However, while the deformation parameter $\mathscr{D}$ increased with an increase in R, it decreased with an increase in S. These observations were justified by inspection of the net normal and tangential electric stresses. In line with shear-driven or buoyancy-driven deformation of drops in creeping flows, here the magnitude of deformation increased with an increase in the viscosity ratio. No tangible changes were observed in the magnitudes of $\mathscr{D}$ and KE as a result of up to one order of magnitude decrease in the density ratio. The effect of the wall on the migration of the drop was studied and it was concluded that drops in region (I), (II-upper), and (II-lower) will be attracted toward the wall, while those in region

(III) will be repelled from the wall. Inspection of the velocity field showed that the hydrodynamic forces were the main factor behind this observation.

References

Baygents, J. C.; Rivette, N. J.; Stone, H. A., (1998): Electrohydrodynamic deformation and interaction of drop pairs. *J. Fluid Mech.,* vol. 368, pp. 359-375.

Behjatian, A.; Esmaeeli, A. (2012): Electrohydrodynamics of a liquid drop in confined domains. *Phys. Rev. E,* vol. 86, pp. 036310.

Esmaeeli, A.; Sharifi, P. (2011): The transient dynamics of a liquid column in a uniform transverse electric field of small strength. *J. Electrostat.,* vol. 69, pp. 504–511.

Esmaeeli, A.; Tryggvason, G. (2004): Computations of film boiling. Part I: numerical method. *Int. J. Heat Mass Transfer,* vol. 47, no. 25, pp. 5451–5461.

Feng, J. Q.; Scott, T. C. (1996): A computational analysis of electrohydrodynamics of a leaky dielectric drop in an electric field. *J. Fluid Mech.,* vol. 311, pp. 289–326.

Lac, E.; Homsy, G. M. (2007): Axisymmetric deformation and stability of a viscous drop in a steady electric field. *J. Fluid Mech.,* vol. 590, pp. 239–264.

Melcher, J. R.; Taylor, G. I. (1969): Electrohydrodynamics: a review of the role of interfacial shear stresses. *Ann. Rev. Fluid Mech.,* vol. 1, pp. 111–147.

Reddy, M. N.; Esmaeeli, A. (2009): The EHD-driven fluid flow and deformation of a liquid jet by a transverse electric field. *Int. J. Multiphase Flow,* vol. 35, pp. 1051–1065.

Rhodes, P. H.; Snyder, R. S.; Roberts, G. O. (1989): Electrohydrodynamic distortion of sample streams in continuous flow electrophoresis. *J. Colloid Int. Sci.,* vol. 129, pp. 78–90.

Saville, D. A. (1997): Electrohydrodynamics: the Taylor-Melcher leaky dielectric model. *Ann. Rev. Fluid Mech.,* vol. 29, pp. 27–64.

Stone, H. A. (1994): Dynamics of drop deformation and breakup in viscous fluids. *Ann. Rev. Fluid Mech.,* vol. 26, pp. 65–102.

Stone, H. A.; Stroock, A. D.; Ajdari, A. (2004): Engineering flows in small devices: Microfluidics toward a lab-on-a-chip. *Ann. Rev. Fluid Mech.,* vol. 36, pp. 381–411.

Taylor, G. I. (1966): Studies in electrohydrodynamics: I. The circulation produced in a drop by an electric field. *Proc. Roy. Soc.,* vol. 291, pp. 159–167.

Torza, S.; Mason, R. G.; Cox, S. G. (1971): Electrohydrodynamic deformation and burst of liquid drops. *Phil Trans. R. Soc. London A,* vol. 269, pp. 295-319.

Tryggvason, G.; Bunner, B.; Esmaeeli, A.; Juric, D.; Al-Rawahi, N.; Tauber, W.; Han, J.; Nas, S.; Jan, Y-J. (2004): A front-tracking method for the computa-

tions of multiphase flow. *J. Computat. Phys.,* vol. 169, no. 2, pp. 708–759.